Polymers **2014**, *6*, 1794-1809; doi:10.3390/polym6061794

OPEN ACCESS

polymers

ISSN 2073-4360

www.mdpi.com/journal/polymers

Article

Fabrication and Characterization of Inorganic Silver and Palladium Nanostructures within Hexagonal Cylindrical Channels of Mesoporous Carbon

Jheng-Guang Li, Cheng-Ying Tsai and Shiao-Wei Kuo *

Department of Materials and Optoelectronic Science, Center for Functional Polymers and Supramolecular Materials, National Sun Yat-Sen University, Kaohsiung 80424, Taiwan;
E-Mails: d983100007@student.nsysu.edu.tw (J.-G.L.); m973100023@student.nsysu.edu.tw (C.-Y.T.)

* Author to whom correspondence should be addressed; E-Mail: kuosw@faculty.nsysu.edu.tw; Tel./Fax: +886-7-525-4099.

Received: 17 February 2014; in revised form: 6 June 2014 / Accepted: 10 June 2014 / Published: 17 June 2014

Abstract: In this study, we prepared a mesoporous carbon with hexagonally packed mesopores through evaporation-induced self-assembly (EISA)—with the diblock copolymer poly(ethylene oxide-*b*-ε-caprolactone) (PEO-*b*-PCL) as the template ($EO_{114}CL_{84}$), phenolic resin as the carbon precursor, hexamethylenetetramine (HMTA) as the curing agent, and star octakis-PEO-functionalized polyhedral oligomeric silsesquioxane (PEO–POSS) as the structure modifier—and subsequent carbonization. We then took the cylindrical mesoporous carbon as a loading matrix, with $AgNO_3$ and $Pd(NO_3)_2$ as metal precursors, to fabricate Ag nanowire/mesoporous carbon and Pd nanoparticle/mesoporous carbon nanocomposites, respectively, through an incipient wetness impregnation method and subsequent reduction under H_2. We used transmission electron microscopy, electron diffraction, small-angle X-ray scattering, N_2 isotherm sorption experiment, Raman spectroscopy, and power X-ray diffraction to investigate the textural properties of these nanometal/carbon nanocomposites. Most notably, the Raman spectra of the cylindrical mesoporous carbon, Ag/mesoporous carbon, and Pd/mesoporous carbon revealed interesting phenomena in terms of the ratios of the intensities of the D and G bands (I_D/I_G), the absolute scattering intensities, and the positions of the D bands.

Keywords: mesoporous carbon; PEO–POSS; inorganic nanometals; Raman spectroscopy

1. Introduction

Evaporation-induced self-assembly (EISA) has been developed aggressively as a strategy for the fabrication of mesoporous nanostructures because of its broad applicability to soft templating using various block copolymer templates [1–12]. Prior to its development, the pore sizes of mesoporous carbons were limited to approximately 5–10 nm as a result of the need for copolymer templates of low molecular weight [13,14]. The EISA method made it feasible to regulate pore structures and pore sizes and allowed the preparation of various mesoporous materials from water-insoluble systems, including mesoporous silicas [2,7,8,10,15–18], mesoporous resins [3,6,9,11], mesoporous TiO_2 [19–21], and mesoporous carbons [2,4,12,16,22–24]. The typical procedure used to prepare ordered mesoporous carbons, so-called "template synthesis" [25–30], involves the use of mesoporous silicas as hard templates, impregnation of carbon precursors into their mesochannels, carbonization under an inert gas, and finally dissolving the hard template of the "ordered mesoporous silica" through etching in $HF_{(aq)}$. Although such template syntheses have been used broadly, they can be ineffective means of fabrication of mesoporous carbons because of the many steps required and complicated processing. To simplify the construction of mesoporous carbons, a clear method through EISA has been developed. Similar to the inorganic/organic assembly of mesoporous silicas, the EISA method can provide great success in the preparation of mesoporous resins and carbons through organic/organic self-assembly. Mesoporous carbons have many potential applications both industrially and scientifically—for example, in adsorption [31–34], separation [32,34], solar cells [35], and electrodes [36]. One of the important applications of mesoporous carbons is their use as matrices for the preparation of nanometal/mesoporous carbon composites [37–41], similar to mesoporous carbons; there has also been some research into the preparation of various nanometal/mesoporous carbon composites for applications in catalysis [42,43] and adsorption [33].

Raman spectroscopy is an excellent method for analyzing the structures and properties of various carbon materials, including active carbon [44], carbon nanotubes [45,46], and mesoporous carbon [47,48]. In addition to the two well-known crystalline structures of natural carbon materials, diamond and graphite, there is a wide range of carbons with disordered forms. In general, two signals that characterize mesoporous carbons typically appear in their Raman spectra: one, near 1582 cm^{-1} (the so-called "G band"), is assigned to the in-plane displacement of carbon atoms in hexagonal carbon sheets, while the other, near 1357 cm^{-1} (the "D band"), is representative of disordered bands of carbon, corresponding to turbostratic carbon layers or very small graphitic domains. The ratio of the intensities of the D and G bands (*i.e.*, I_D/I_G) can provide information relating to the degree of graphitization; for example, a lower value of I_D/I_G corresponds to a higher degree of graphitization [38,43,47–49]. The Raman signals of mesoporous carbon can be enhanced by the effect of the surface plasmon resonance of Ag nanoparticles [39,50]; in addition, the locations of the Raman signals of Pd-doped carbon materials are typically slightly lower than those of pure graphitic materials and also lower than those reported for ordered mesoporous carbons synthesized using the hard-template method, presumably because of the minor disorientation of the carbon-containing molecules during the self-template method [33]. Therefore, a Raman spectrum can reveal not only the degree of graphitization of a pure mesoporous carbon but also the effects of interactions between various nanometals and the carbon matrix.

The related studies of Ag/mesoporous carbon nanocomposites also received much attention recently. For example, Jaroniec *et al.* prepared soft-templating synthesis of ordered mesoporous carbons (OMCs) in the presence of tetraethyl orthosilicate (TEOS), and silver nitrate was carried out in order to introduce silver nanoparticles and to create additional microporosity in these materials [51]. Huang *et al.* studied the ordered mesoporous carbon-reduced graphene oxide (OMC-RGO) composites that are prepared through the organic-organic self-assembly method [52]. Lu *et al.* displayed the Ag nanoparticles (Ag NPs) supported on nitrogen-doped ordered mesoporous carbon (N-OMC) were fabricated by one-pot synthesis strategy, in which 2D hexagonally ordered mesoporous SBA-15 and aniline were used as template and carbon precursor, respectively [53]. Compared to the related studies recently, we have discussed the properties of unique Ag/mesoporous carbon nanocomposites that took our mesoporous phenolic resin with typical hexagonal cylindrical structures as the carbon sources.

In previous studies, we employed EISA—with the diblock copolymer poly(ethylene oxide-*b*-ε-caprolactone) (PEO-*b*-PCL) as the template, phenolic resin as the matrix precursor, and hexamethylenetetramine (HMTA) as the curing agent—to prepare a series of mesoporous phenolic resins [6]. Moreover, we blended in the star octakis-PEO-functionalized polyhedral oligomeric silsesquioxane (PEO–POSS) to induce higher ordering of the mesostructures as well as mesophase transformations of the mesoporous phenolic structures [9]. In this present study, we used a mesoporous phenolic resin possessing a hexagonal cylindrical structure as the carbon precursor for the preparation of mesoporous carbon under a N_2 atmosphere at 800 °C; subsequently, we employed this product and a simple incipient wetness strategy to fabricate Ag/mesoporous carbon and Pd/mesoporous carbon nanocomposites (Scheme 1). We have used transmission electron microscopy (TEM), small-angle X-ray scattering (SAXS), N_2 adsorption/desorption isotherms, electron diffraction, Raman spectroscopy, and power X-ray diffraction (XRD) to characterize all of these mesoporous carbon and metal/carbon samples.

Scheme 1. Preparation of mesoporous phenolic, mesoporous carbon, and metal/mesoporous carbon.

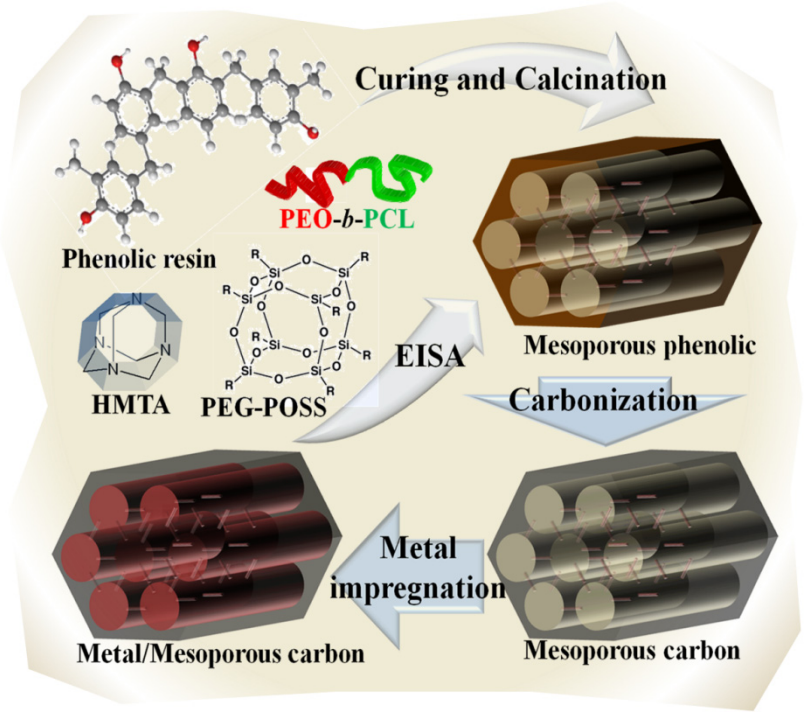

2. Experimental Section

2.1. Materials

Monomethoxy-poly(ethylene glycol) having a molecular weight of 5000 (PEO_{114}) was obtained from Fluka (Buchs, Switzerland). ε-Caprolactone (ε-CL, Acros, St. Louis, MO, USA) was purified through vacuum distillation over CaH_2. Stannous(II) octoate ($Sn(Oct)_2$, Sigma, St. Louis, MO, USA) was used as received. Star PEO–POSS (molecular weight: 5576 g/mol) was purchased from Hybrid Plastics (Hattiesburg, MS, USA). Silver nitrate ($AgNO_3$) and palladium(II) nitrate dehydrate were purchased from Aldrich (St. Louis, MO, USA). The phenolic was synthesized through a condensation reaction with H_2SO_4, producing a material with an average molecular weight (M_n = 500) similar to those described previously [6], EtOH (95%) and tetrahydrofuran (THF, >99%) were purchased from ECHO (Kaohsiung, Taiwan). Diblock copolymers were prepared through the ring-opening polymerization (ROP) of ε-CL in the presence of PEO_{114} and $Sn(Oct)_2$. The reaction mixtures were prepared by introducing a desired volume of ε-CL monomer into a silanized flask containing a pre-weighed amount of PEO_{114} under a N_2 atmosphere. Several drops of $Sn(Oct)_2$ were added and then the flask was connected to a vacuum line, evacuated, sealed off, and heated at 130 °C. After 24 h, the resulting block copolymers were dissolved in CH_2Cl_2 and precipitated in an excess of cold *n*-hexane. The polymers were dried at 40 °C under vacuum.

2.2. Mesoporous Carbons Templated by PEO-b-PCL Copolymers

Mesoporous carbons were prepared using an EISA strategy with PEO-*b*-PCL as the template, THF as the solvent, and phenolic resin as the carbon source. In a typical synthesis, phenolic resin, HMTA, $EO_{114}CL_{84}$ (M_n = 14,600; PDI = 1.31), and star PEO–POSS were mixed in THF until the solution became homogenous. The THF was evaporated slowly at room temperature and then the sample was vacuum-dried at 30 °C for 1 day. Curing of the samples was performed under the following temperature profile: 100 °C for 2 h, then 150 °C for 2 h, and then 190 °C for 2 h. Pyrolysis of the crosslinked samples was performed in a tubular furnace under N_2 at 800 °C for 3 h at a heating rate of 5 °C/min.

2.3. Metal/Mesoporous Carbon Composites

To prepare nanometals within nanoscale channels, a mesoporous carbon powder having a specific structure (20 mg) was soaked in a tiny amount of a saturated solution of the metal precursor (ca. 13 mg of metal precursor in several drops of water). The product was filtered off, quickly rinsed with a little EtOH, and subjected to thermal treatment to decompose the impregnated metal precursor and form the metal nanostructures (reduction conditions for Ag: 250 °C for 1 h, heating at a rate of 1 °C/min to 350 °C, and then maintaining that temperature for 2 h; for Pd: 75 °C for 0, 2, or 4 h, then heating at 1 °C/min to 200 °C, and then maintaining that temperature for 2 h; atmosphere: 10% H_2 and 90% N_2).

2.4. Characterization

^{1}H-NMR spectra were recorded at room temperature using a Bruker AM 500 (500 MHz) spectrometer (Taipei, Taiwan), with the residual proton resonance of the deuterated solvent acting as the internal standard. Molecular weights were determined through gel permeation chromatography (GPC) using a Waters 510 high-performance liquid chromatograph equipped with a 410 differential refractometer (Milford, MA, USA) and three Ultrastyragel columns (100, 500, and 10^3 Å) (Hewlett Packard, Avondale, PA, USA), with dimethylformamide (DMF) as the eluent (flow rate: 0.4 mL/min). SAXS was performed using a NANOSTAR U small-angle X-ray scattering system (Bruker AXS, Karlsruhe, Germany) and Cu K_α radiation (30 W, 50 kV, 600 μA). The *d*-spacings were calculated using the formula:

$$d = 2\pi/q \quad (1)$$

where q is the scattering vector. TEM images were recorded using a JEOL 3010 microscope (Tokyo, Japan) operated at 200 kV; samples for TEM measurement were suspended in EtOH and supported onto a holey carbon film on a Cu grid. Nitrogen adsorption/desorption isotherms were measured at −196 °C using an ASAP 2020 analyzer (Micromeritics, Norcross, GA, USA); prior to measurements, the samples were degassed under vacuum at 200 °C for at least 6 h. The Brunauer–Emmett–Teller (BET) method was used to calculate the specific surface areas and pore volumes; pore size distributions were derived from the adsorption branches of the isotherms by using the Barrett–Joyner–Halenda (BJH) model. XRD patterns were recorded using a German Bruker AXS D8 ADVANCE X-ray diffractometer and Cu K_α radiation (λ = 1.541 Å) over a 2θ range from 30° to 90° (Taipei, Taiwan). Raman spectra were recorded using a Jobin-Yvon T6400 micro-Raman system (Tokyo, Japan) with the 325 nm line of a He–Cd laser as the excitation source at room temperature.

3. Results and Discussion

3.1. Silver Nanowires within Mesochannels of Hexagonal Cylindrical Mesoporous Carbon

To begin the study, we required a mesoporous carbon for use as the matrix for the construction of the nanometal/mesoporous carbon nanocomposites. To prepare the mesoporous carbon, we first used a simple ring-opening polymerization (ROP) to synthesize an amphiphilic diblock copolymer PEO–PCL, with a specific weight ratio of each segment ($EO_{114}CL_{84}$; NMR M_n = 14,600; PDI = 1.31) [5,6]. Next, we combined the $EO_{114}CL_{84}$, phenolic resin, and PEO–POSS at a unique weight ratio ($EO_{114}CL_{84}$:phenolic resin:PEO–POSS = 50:50:22) and subjected the mixture to EISA and calcination steps to fabricate an hexagonal cylindrical mesoporous phenolic resin [9]. Finally, we carbonized our hexagonal cylindrical mesoporous carbon under a N_2 atmosphere. With the mesoporous carbon in hand, we impregnated the Ag precursor ($AgNO_3$) inside the hexagonal mesochannels by means of capillary force and then applied a reduction under H_2 to obtain the Ag/mesoporous carbon nanocomposite. Figure 1a presents the SAXS patterns of the mesoporous carbon and the Ag/mesoporous carbon. For the mesoporous carbon, we observe one sharp primary peak and another ill-secondary peak, with an approximate ratio (q) of 1: $\sqrt{3}$, consistent with hexagonally packing. After impregnation of the Ag nanowires, the primary reflection peak underwent an apparent collapse, consistent with a certain

degree of infilling of the Ag nanowires within the hexagonal mesochannels; in other words, imperfect infilling of the Ag precursors occurred during the impregnation step. For further confirmation of these phenomena, Figure 1b–e displays TEM images of the mesoporous carbon (Figure 1b,c) and Ag/mesoporous carbon (Figure 1d,e) viewed from the side of the hexagonal cylindrical structures (*i.e.*, viewed from the (10) plane). Consistent with the SAXS data, the TEM image of the mesoporous carbon was typical of that expected for a side view of hexagonal packing (Figure 1b,c); on the other hand, some Ag nanowires were evident in Figure 1d,e, suggesting successful impregnation of the Ag nanowires within the hexagonal mesopores of the mesoporous carbon sample.

Figure 1. (**a**) SAXS patterns of the hexagonal cylindrical mesoporous carbon and the Ag/cylindrical carbon; (**b**–**e**) TEM images of (**b**,**c**) the hexagonal cylindrical mesoporous carbon and (**d**,**e**) the Ag/cylindrical carbon.

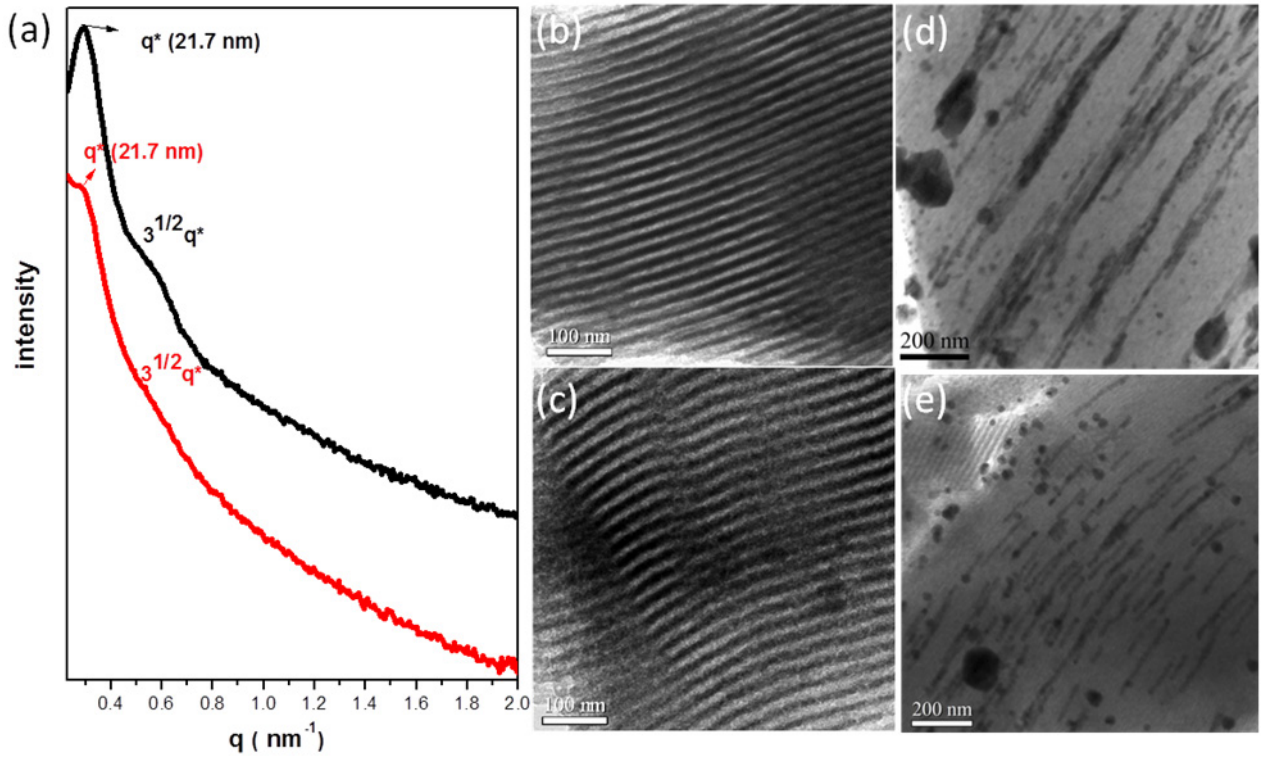

Figure 2 presents a TEM image of the Ag nanowires within the cylindrical mesopores (Figure 2a) and the corresponding selected-area electron diffraction pattern (Figure 2b); we observed polycrystalline distribution characteristics for the Ag metal, consistent with the indistinct diffraction rings of the (111), (200), (220), and (311) planes. XRD analysis of the Ag/mesoporous carbon sample revealed signals for the Ag metallic phase, representing the (111), (200), (220), and (311) reflections, respectively, upon increasing the value of 2θ (Figure 2c). The N_2 sorption isotherms of the two mesoporous carbon samples are representative type-IV curves featuring one capillary condensation step (Figure 3a) and H_1-like hysteresis loops, suggesting that the two mesoporous structures had cylinder-like pores (consistent with the TEM images and SAXS patterns). Figure 3b reveals that the pore sizes of the two samples were distributed in the approximate range 19.4–19.7 nm, as measured from the adsorption branches based on the Harkins–Jura model. The infilling ratio of Ag metal within the cylindrical mesopores was approximately 44%, calculated from the difference in pore volumes between the

mesoporous carbon and the Ag/mesoporous carbon. Table 1 lists the textural properties of sample 1 (cylindrical mesoporous carbon) and sample 2 (Ag/mesoporous carbon).

Figure 2. (**a**) TEM images; (**b**) selected-area electron diffraction pattern; and (**c**) powder XRD pattern of the Ag/cylindrical mesoporous carbon.

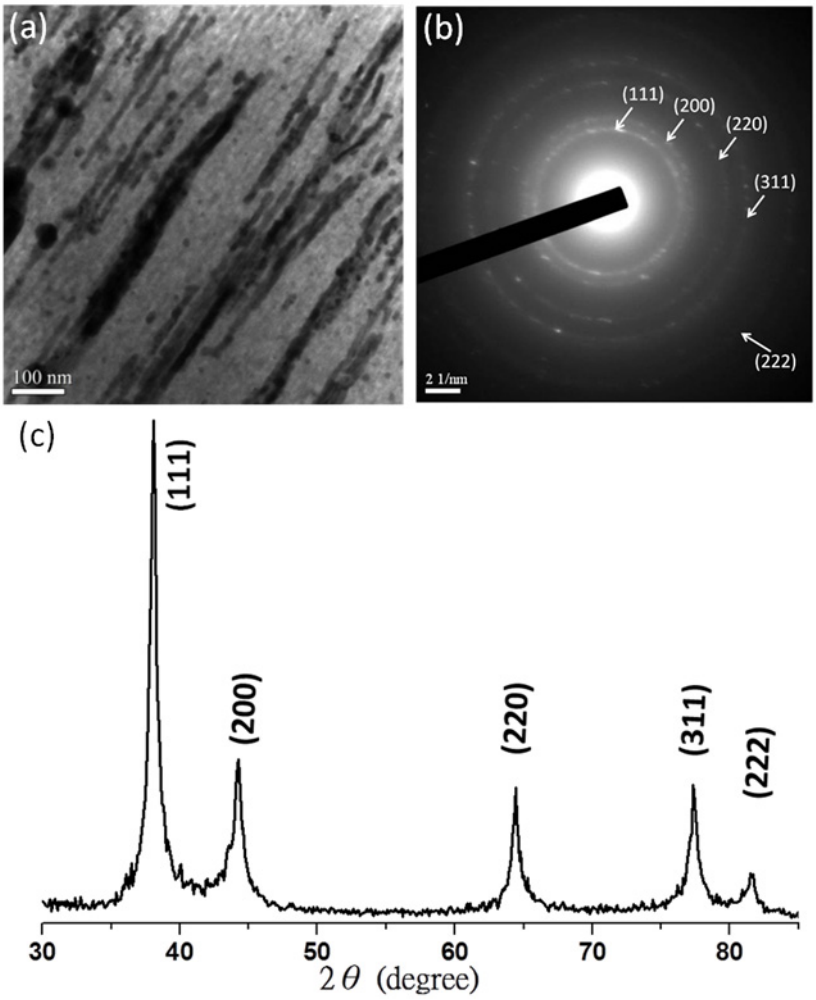

Table 1. Textural properties of the mesoporous carbon and metal/mesoporous carbon samples.

Sample	*d* (nm) [a]	Pore size (nm)	S_{BET} (m^2/g) [b]	S_M (m^2/g) [b]	Pore volume (cm^3/g)	Micropore volume (cm^3/g)	Note	I_D/I_G [c]	Infilling ratio (%) [d]
1	21.7	17.4	729	515	0.70	0.239	Cylindrical mesoporous carbon	0.996	–
2	21.7	17.6	409	286	0.39	0.133	Ag/mesoporous carbon	1.116	44
3	21.7	17.4	660	468	0.62	0.218	Pd/mesoporous carbon	1.009	11

Notes: [a] The d-spacings were calculated using the formula $d = 2\pi/q$, [b] S_{BET} and S_M are the total BET surface area and micropore surface area calculated from the *t*-plots, respectively; [c] I_D/I_G was calculated from the intensity of the D and G bands in the Raman spectra; [d] Infilling ratio (%) = [pore volume (mesoporous carbon) − pore volume (nanocomposite)]/pore volume (mesoporous carbon).

Figure 3. (**a**) N_2 adsorption/desorption isotherms and (**b**) pore size distribution curves of the hexagonal cylindrical mesoporous carbon and the Ag/cylindrical carbon.

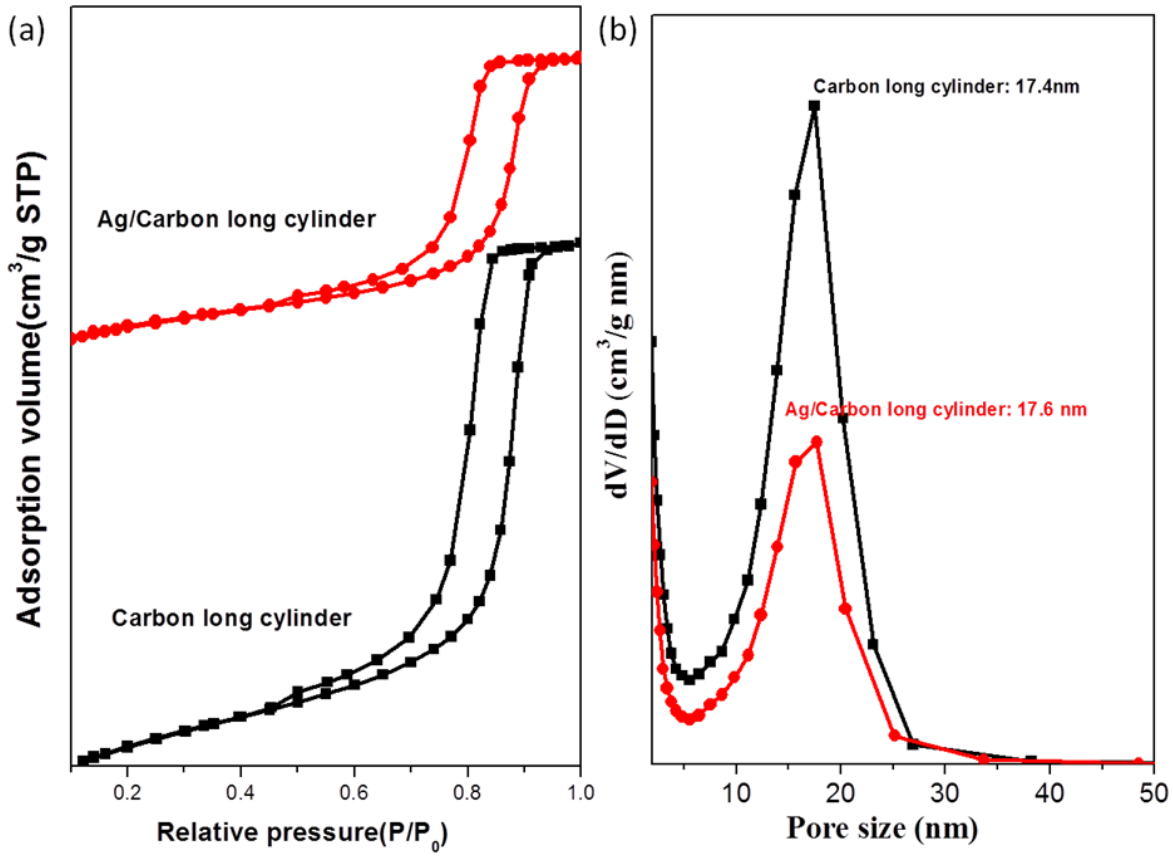

3.2. Palladium Nanometals within Mesochannels of Hexagonal Cylindrical Mesoporous Carbon

For comparison with the Ag/mesoporous carbon system, we also prepared a Pd/mesoporous carbon nanocomposite using a similar procedure. Initially, we took advantage of capillary forces to permeate tiny amounts of $Pd(NO_3)_{2(aq)}$ into the pores of the mesoporous carbon through an incipient wetness impregnation method; after calcination and reduction under H_2, we obtained the Pd/mesoporous carbon. The infilling amount of the Pd nanometal was, however, too low to affect the original structure; as revealed in Figure 4a, the signals in the SAXS pattern of the Pd/mesoporous carbon were merely slightly weaker than those of the original reflection peaks of the mesoporous carbon. TEM images of the mesoporous carbon (Figure 4b,c) and the Pd/mesoporous carbon (Figure 4d,e) provided evidence for the existence of nanostructures. Consistent with the SAXS data, after impregnation of the Pd nanometal, some fragmentary Pd nanoparticles were dispersed within the hexagonally packed mesopores. We suggest two main reasons for the loading ratio of Pd being much lower than that of Ag:the solubility of the Pd precursor is lower than that of $AgNO_3$ in water and the interaction between $Pd(NO_3)_2$ and the carbon surface is weaker than that between $AgNO_3$ and the carbon surface.

Figure 4. (**a**) SAXS patterns of the hexagonal cylindrical mesoporous carbon and the Pd/cylindrical silica; (**b**–**e**) TEM images of (**b**,**c**) the hexagonal cylindrical mesoporous carbon and (**d**,**e**) the Pd/cylindrical carbon.

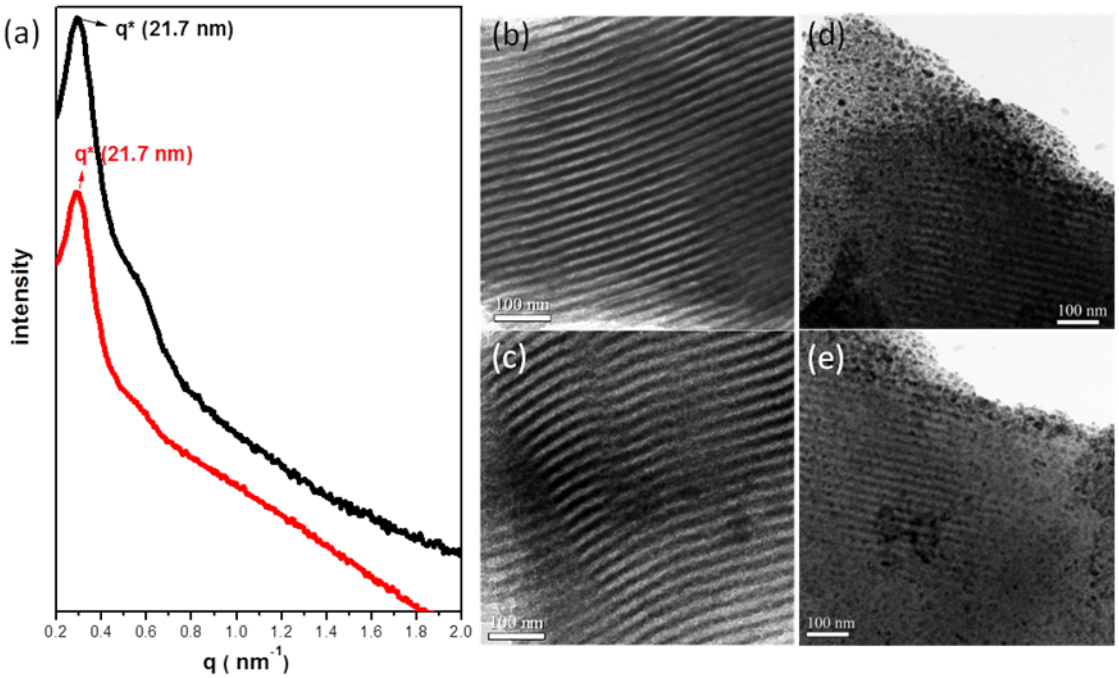

Figure 5. (**a**) TEM images; (**b**) selected-area electron diffraction pattern; and (**c**) powder XRD pattern of the Ag/cylindrical mesoporous carbon prepared.

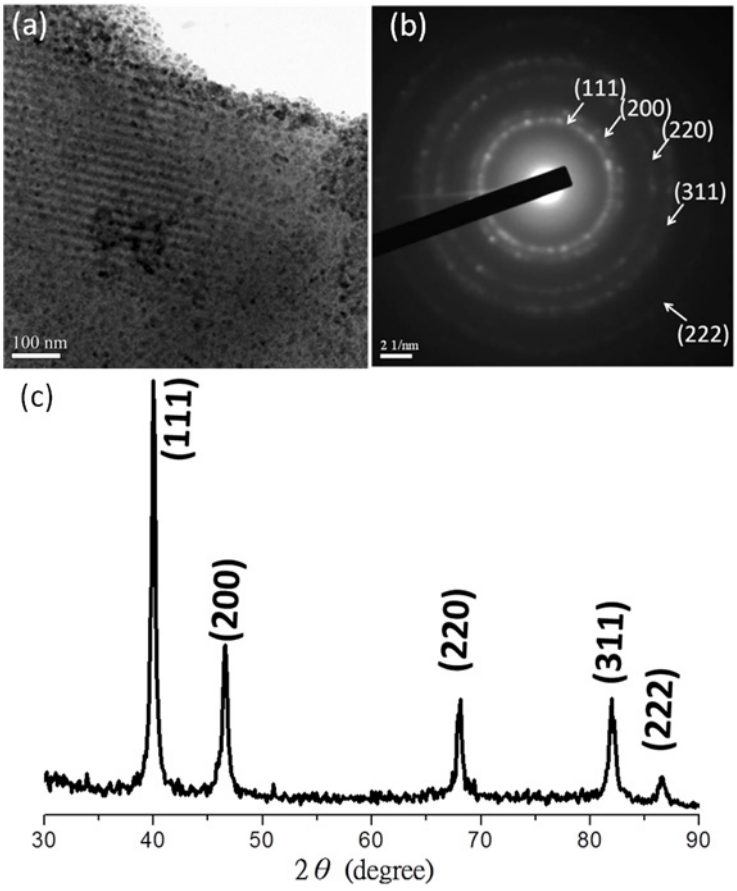

To obtain more information about the Pd/mesoporous carbon composite (Figure 5a), Figure 5b,c displays the electron diffraction and XRD analyses, respectively. In Figure 5b,c, the typical metallic Pd reflections, indicated as (111), (200), (220), (311), and (222), respectively, suggest that the Pd precursor had been reduced completely to form Pd nanostructures. The N_2 sorption isotherms (Figure 6) of sample 3 (Pd/mesoporous carbon) are representative type-IV curves with sharp capillary condensation steps in the relative pressure range from 0.85 to 0.90, suggesting a regular mesostructure. Similar to that of sample 1 (cylindrical mesoporous carbon), the hysteresis loop exhibits a definite H_1-like shape and a pore size of approximately 17.4 nm, measured based on the Harkins–Jura model. From the difference in pore volumes between samples 1 and 3 (Table 1), we calculate an infilling ratio of 11%; Table 1 lists all of the other textural properties of sample 3.

Figure 6. (**a**) N_2 adsorption/desorption isotherms and (**b**) pore size distribution curves of the hexagonal cylindrical mesoporous carbon and the Pd/cylindrical carbon.

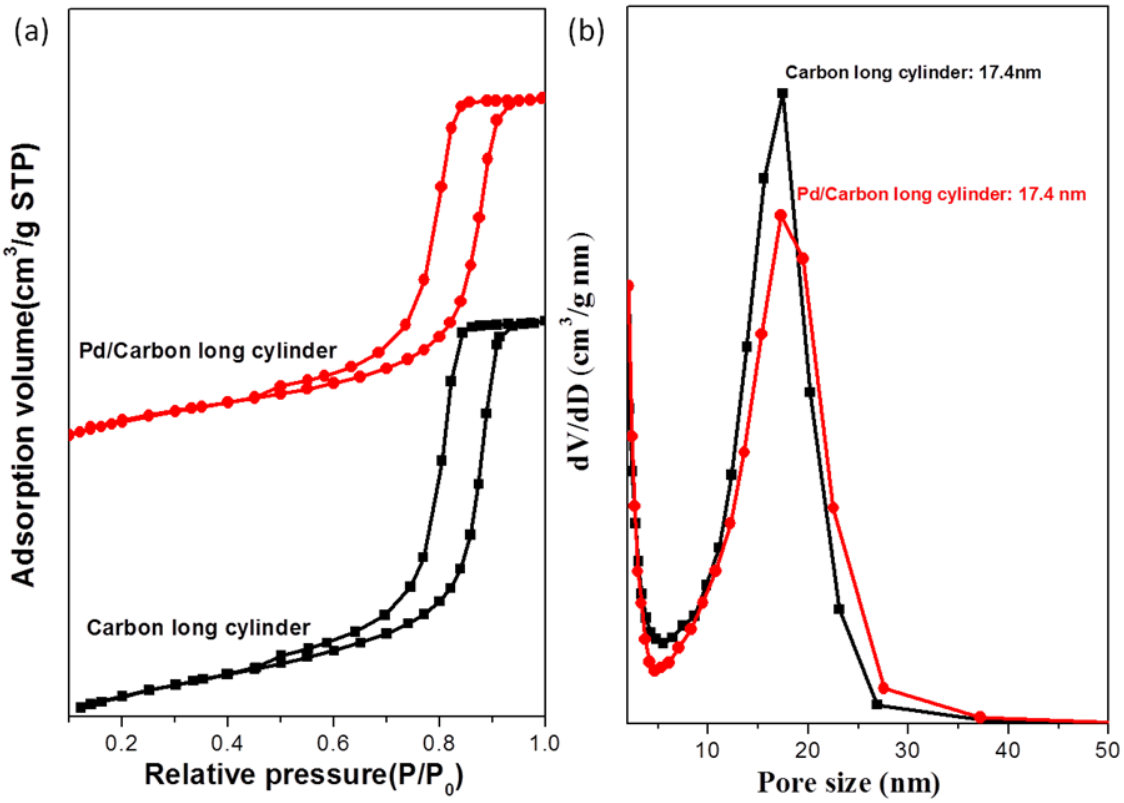

3.3. Raman Spectra of Mesoporous Carbon and Nanometal/Mesoporous Carbon Samples

Figure 7 presents Raman spectra of the mesoporous carbon and the nanometal/mesoporous carbon samples from 1000 to 2000 cm^{-1}. Three interesting features appear in these Raman spectra. The first is related to the ratio I_D/I_G (ratio of intensities of the D and G bands) of the different samples; the accuracy of intensity ratio is doubtful owing to the lack of baseline correction, in other words, the absolute value of I_D/I_G is meaningless, however, we could still determine the tendency of the degree of graphitization by the ratio I_D/I_G. Second, variations in the absolute scattering intensities of the different carbon samples (mesoporous carbon, Ag/mesoporous carbon, and Pd/mesoporous carbon) reveal the different interactions between the nanometals and the mesoporous carbons. Third, we look at the location

and intensity of the D bands in the Raman spectra of the three samples. We observed two peaks between 1000 and 2000 cm^{-1} in the Raman spectra that we could attribute to the D band (*ca.* 1312 cm^{-1}) and G band (*ca.* 1587 cm^{-1}). The D band is typically representative of disordered carbon, corresponding to turbostratic carbon layers or very small graphitic domains; the G band is mainly assigned to in-plane displacement of carbon atoms in hexagonal carbon sheets [47–49]. Accordingly, the I_D/I_G ratio can be taken as reference for the variation of degree of graphitization. Table 1 lists the I_D/I_G ratios of the three samples: 0.996 for mesoporous carbon, 1.116 for Ag/mesoporous carbon, and 1.009 for the Pd/mesoporous carbon. Despite the I_D/I_G ratios, we could not find conclusive evidence for the degree of graphitization, but the variation of peak height is still apparent in Figure 7, especially for the Ag/mesoporous carbon sample. Some information could be gleaned from these values because we prepared our nanometal/mesoporous carbon samples from the same mesoporous carbon material. Clearly, the I_D/I_G ratios of the nanometal/mesoporous carbon samples were higher than that of the pure mesoporous carbon, illustrating that the addition of nanometals within the mesochannels decreased the degree of graphitization, implying that the graphitiferous carbon atoms used their π electrons to coordinate the nanometals. The effect of the Ag nanowires was stronger than that of the Pd nanoparticles simple because the infilling ratio of the Ag nanowires (44%) was much larger than that of the Pd nanoparticles (11%). Next, the scattering intensity of the Ag/mesoporous carbon was much higher than that of the mesoporous carbon or the Pd/mesoporous carbon; this behavior is consistent with the Raman signals of other mesoporous carbons having been enhanced as a result of the surface plasmon resonance of Ag nanoparticles [39,50]. In addition, the locations of the D bands in our samples 1–3 (*ca.* 1312 cm^{-1}) were slightly lower than those of pure graphitic materials and other reported ordered mesoporous carbons (typically *ca.* 1350 cm^{-1}). We attribute these shifts to the minor disorientation of the carbon molecules during the self-templation method [33].

Figure 7. Raman spectra of mesoporous carbon (black line), Pd/mesoporous carbon (red line), and Ag/mesoporous carbon (blue line).

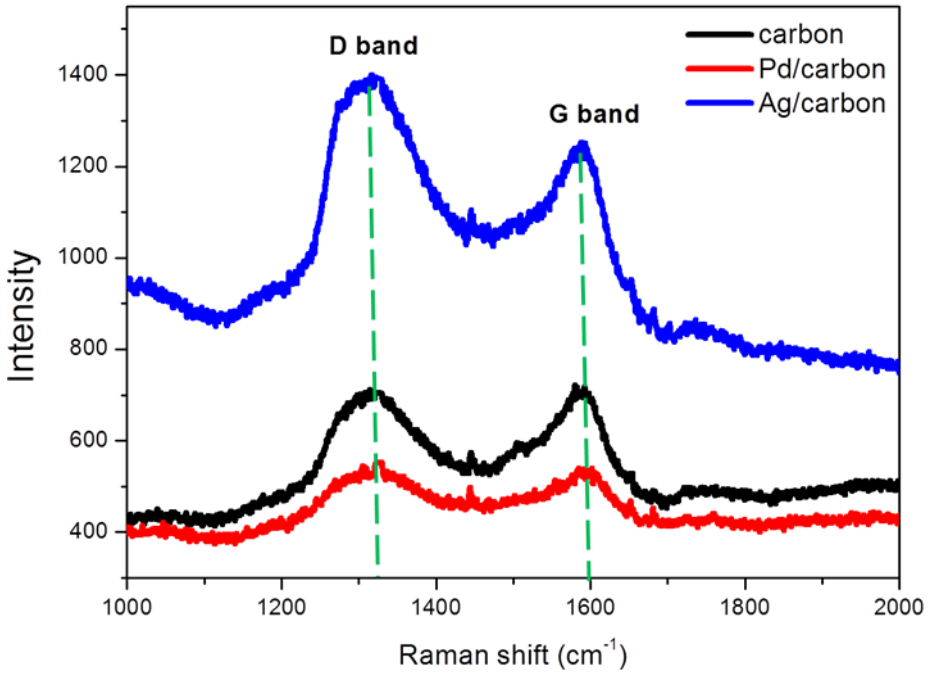

4. Conclusions

Through regulation of the weight ratio of phenolic, $EO_{114}CL_{84}$, and PEO–POSS (50:50:22), we have successfully fabricated a cylindrical mesoporous carbon using the EISA method; we then used this material to prepare Ag/mesoporous carbon and Pd/mesoporous carbon nanocomposites, after impregnation of metal precursors under capillary force and thermo-reduction under a H_2 atmosphere (10% H_2 and 90% N_2). TEM images revealed the morphologies of the nanocomposites; for Ag/carbon, we observed well-defined Ag nanowires within the cylindrical mesopores; in contrast, the Pd/carbon sample featured a poor infilling ratio (11%) with only a few disperse nanoparticles located within the mesochannels. These features were reflected in the Raman spectra of samples 1–3: the Ag/mesoporous carbon provided the highest I_D/I_G ratio (due to the lower degree of graphitization as a result of greater coordination of the Ag nanometals by the π electrons of the carbon atoms) and also the strongest scattering intensity (as a result of the signal enhancement effect of the surface plasmon resonance of the Ag nanowires).

Acknowledgment

This study was supported financially by the National Science Council, Taiwan, under contracts NSC 100-2221-E-110-029-MY3 and NSC-100-2628-E-110-001.

Author Contributions

Jheng-Guang Li, contributed to the analysis of the data and writing of the paper; Cheng-Ying Tsai synthesizes the mesoporous materials and carried out the analyses; Shiao-Wei Kuo coordinated the study, interpreted the results and discussion and contributed to the writing of the paper.

Conflicts of Interest

The authors declare no conflict of interest.

References

1. Soler-Illia, G.; Crepaldi, E.L.; Grosso, D.; Sanchez, C. Block copolymer-templated mesoporous oxides. *Curr. Opin. Coll. Interface Sci.* **2003**, *8*, 109–126.
2. Deng, Y.H.; Yu, T.; Wan, Y.; Shi, Y.F.; Meng, Y.; Gu, D.; Zhang, L.J.; Huang, Y.; Liu, C.; Wu, X.J.; *et al.* Ordered mesoporous silicas and carbons with large accessible pores templated from amphiphilic diblock copolymer poly(ethylene oxide)-*b*-polystyrene. *J. Am. Chem. Soc.* **2007**, *129*, 1690–1697.
3. Valkama, S.; Nykanen, A.; Kosonen, H.; Ramani, R.; Tuomisto, F.; Engelhardt, P.; ten Brinke, G.; Ikkala, O.; Ruokolainen, J. Hierarchical porosity in self-assembled polymers: Post-modification of block copolymer–phenolic resin complexes by pyrolysis allows the control of micro- and mesoporosity. *Adv. Funct. Mater.* **2007**, *17*, 183–190.

4. Zhang, J.Y.; Deng, Y.H.; Wei, J.; Sun, Z.K.; Gu, D.; Bongard, H.; Liu, C.; Wu, H.H.; Tu, B.; Schuth, F.; *et al.* Design of amphiphilic ABC triblock copolymer for templating synthesis of large-pore ordered mesoporous carbons with tunable pore wall thickness. *Chem. Mater.* **2009**, *21*, 3996–4005.
5. Li, J.G.; Kuo, S.W. Phase behavior of mesoporous nanostructures templated by amphiphilic crystalline–crystalline diblock copolymers of poly(ethylene oxide-*b*-ε-caprolactone). *RSC Adv.* **2011**, *1*, 1822–1833.
6. Li, J.G.; Lin, Y.D.; Kuo, S.W. From Microphase separation to self-organized mesoporous phenolic resin through competitive hydrogen bonding with double-crystalline diblock copolymers of poly(ethylene oxide-*b*-ε-caprolactone). *Macromolecules* **2011**, *44*, 9295–9309.
7. Li, J.G.; Chang, Y.H.; Lin, Y.S.; Kuo, S.W. Templating amphiphilic poly(ethylene oxide-*b*-ε-caprolactone) diblock copolymers provides ordered mesoporous silicas with large tunable pores. *RSC Adv.* **2012**, *2*, 12973–12982.
8. Li, J.G.; Chen, W.C.; Kuo, S.W.S. Phase behavior of mesoporous silicas templated by the amphiphilic diblock copolymer poly(ethylene-*b*-ethylene oxide). *Microporous Mesoporous Mater.* **2012**, *163*, 34–41.
9. Li, J.G.; Chung, C.Y.; Kuo, S.W. Transformations and enhanced long-range ordering of mesoporous phenolic resin templated by poly(ethylene oxide-*b*-ε-caprolactone) block copolymers blended with star poly(ethylene oxide)-functionalized silsesquioxane (POSS). *J. Mater. Chem.* **2012**, *22*, 18583–18595.
10. Li, J.G.; Lin, R.B.; Kuo, S.W. Hierarchical mesoporous silica fabricated from an ABC triblock terpolymer as a single template. *Macromol. Rapid Commun.* **2012**, *33*, 678–682.
11. Chu, W.C.; Li, J.G.; Kuo, S.W. From flexible to mesoporous polybenzoxazine resins templated by poly(ethylene oxide-*b*-ε-caprolactone) copolymer through reaction induced microphase separation mechanism. *RSC Adv.* **2013**, *3*, 6485–6498.
12. Wickramaratne, N.P.; Jaroniec, M. Phenolic resin-based carbons with ultra-large mesopores prepared in the presence of poly(ethylene oxide)–poly(butylene oxide)–poly(ethylene oxide) triblock copolymer and trimethyl benzene. *Carbon* **2013**, *51*, 45–51.
13. Meng, Y.; Gu, D.; Zhang, F.Q.; Shi, Y.F.; Yang, H.F.; Li, Z.; Yu, C.Z.; Tu, B.; Zhao, D.Y. Ordered mesoporous polymers and homologous carbon frameworks: Amphiphilic surfactant templating and direct transformation. *Angew. Chem. Int. Ed.* **2005**, *44*, 7053–7059.
14. Meng, Y.; Gu, D.; Zhang, F.Q.; Shi, Y.F.; Cheng, L.; Feng, D.; Wu, Z.X.; Chen, Z.X.; Wan, Y.; Stein, A.; *et al.* A Family of highly ordered mesoporous polymer resin and carbon structures from organic–organic self-assembly. *Chem. Mater*. **2006**, *18*, 4447–4464.
15. Lee, Y.F.; Chang, K.H.; Chu, C.Y.; Chen, H.L.; Hu, C.C. Microstructure tuning of mesoporous silica prepared by evaporation-induced self-assembly processes: Interactions among solvent evaporation, micelle formation/packing and sol condensation. *RSC Adv.* **2011**, *1*, 401–407.
16. Wei, H.; Lv, Y.Y.; Han, L.; Tu, B.; Zhao, D.Y. Facile synthesis of transparent mesostructured composites and corresponding crack-free mesoporous carbon/silica monoliths. *Chem. Mater.* **2011**, *23*, 2353–2360.

17. De Los Cobos, O.; Fousseret, B.; Lejeune, M.; Rossignol, F.; Dutreilh-Colas, M.; Carrion, C.; Boissiere, C.; Ribot, F.; Sanchez, C.; Cattoen, X.; *et al.* Tunable multifunctional mesoporous silica microdots arrays by combination of inkjet printing, EISA, and click chemistry. *Chem. Mater.* **2012**, *24*, 4337–4342.
18. Vaid, C.; Murugavel, S.; Kashayap, R.; Tandon, R.P. Synthesis and *in vitro* bioactivity of surfactant templated mesoporous sodium silicate glasses. *Microporous Mesoporous Mater.* **2012**, *159*, 17–23.
19. Ba, J.H.; Polleux, J.; Antonietti, M.; Niederberger, M. Non-aqueous synthesis of tin oxide nanocrystals and their assembly into ordered porous mesostructures. *Adv. Mater.* **2005**, *17*, 2509.
20. Das, S.K.; Bhunia, M.K.; Bhaumik, A. Self-assembled TiO_2 nanoparticles: Mesoporosity, optical and catalytic properties. *Dalton Trans.* **2010**, *39*, 4382–4390.
21. Soler-Illia, G.; Louis, A.; Sanchez, C. Synthesis and characterization of mesostructured titania-based materials through evaporation-induced self-assembly. *Chem. Mater.* **2002**, *14*, 750–759.
22. Chaichanawong, J.; Yamamoto, T.; Kataoka, S.; Endo, A.; Ohmori, T. Synthesis of monodisperse carbonaceous beads with ordered mesoporous structure. *Carbon* **2009**, *47*, 929–932.
23. Hu, D.; Xu, Z.; Zeng, K.; Zheng, S. From self-organized novolac resins to ordered nanoporous carbons. *Macromolecules* **2010**, *43*, 2960–2969.
24. Huang, C.H.; Doong, R.A. Sugarcane bagasse as the scaffold for mass production of hierarchically porous carbon monoliths by surface self-assembly. *Microporous. Mesoporous Mater.* **2012**, *147*, 47–52.
25. Ryoo, R.; Joo, S.H.; Kruk, M.; Jaroniec, M. Ordered mesoporous carbons. *Adv. Mater.* **2001**, *13*, 677–681.
26. Han, S.J.; Hyeon, T. Simple silica-particle template synthesis of mesoporous carbons. *Chem. Commun.* **1999**, 1955–1956.
27. Fuertes, A.B. Template synthesis of mesoporous carbons with a controlled particle size. *J. Mater. Chem.* **2003**, *13*, 3085–3088.
28. Kruk, M.; Dufour, B.; Celer, E.B.; Kowalewski, T.; Jaroniec, M.; Matyjaszewski, K. Synthesis of mesoporous carbons using ordered and disordered mesoporous silica templates and polyacrylonitrile as carbon precursor. *J. Phys. Chem. B* **2005**, *109*, 9216–9225.
29. Lu, A.H.; Li, W.C.; Schmidt, W.; Schuth, F. Template synthesis of large pore ordered mesoporous carbon. *Microporous. Mesoporous Mater.* **2005**, *80*, 117–128.
30. Yang, C.M.; Weidenthaler, C.; Spliethoff, B.; Mayanna, M.; Schuth, F. Facile template synthesis of ordered mesoporous carbon with polypyrrole as carbon precursor. *Chem. Mater.* **2005**, *17*, 355–358.
31. Zhuang, X.; Wan, Y.; Feng, C.M.; Shen, Y.; Zhao, D.Y. Highly efficient adsorption of bulky dye molecules in wastewater on ordered mesoporous carbons. *Chem. Mater.* **2009**, *21*, 706–716.
32. Liang, C.D.; Li, Z.J.; Dai, S. Mesoporous carbon materials: Synthesis and modification. *Angew. Chem. Int. Ed.* **2008**, *47*, 3696–3717.
33. Saha, D.; Deng, S.G. Hydrogen adsorption on ordered mesoporous carbons doped with Pd, Pt, Ni, and Ru. *Langmuir* **2009**, *25*, 12550–12560.

34. Yin, Y.Y.; Zhou, S.X.; Min, C.; Wu, L.M. Preparation of rattle-type magnetic mesoporous carbon spheres and their highly efficient adsorption and separation. *J. Colloid. Interface Sci.* **2011**, *361*, 527–533.
35. Wang, G.Q.; Xing, W.; Zhuo, S.P. Application of mesoporous carbon to counter electrode for dye-sensitized solar cells. *J. Power Sources* **2009**, *194*, 568–573.
36. Numao, S.; Judai, K.; Nishijo, J.; Mizuuchi, K.; Nishi, N. Synthesis and characterization of mesoporous carbon nano-dendrites with graphitic ultra-thin walls and their application to supercapacitor electrodes. *Carbon* **2009**, *47*, 306–312.
37. Fulvio, P.F.; Liang, C.D.; Dai, S.; Jaroniec, M. Mesoporous carbon materials with ultra-thin pore walls and highly dispersed nickel nanoparticles. *Eur. J. Inorg. Chem.* **2009**, *2009*, 605–612.
38. Su, F.B.; Zhao, X.S.; Wang, Y.; Zeng, J.H.; Zhou, Z.C.; Lee, J.Y. Synthesis of graphitic ordered macroporous carbon with a three-dimensional interconnected pore structure for electrochemical applications. *J. Phys. Chem. B* **2005**, *109*, 20200–20206.
39. Chi, Y.; Zhao, L.; Yuan, Q.; Yan, X.; Li, Y.J.; Li, N.; Li, X.T. *In situ* auto-reduction of silver nanoparticles in mesoporous carbon with multifunctionalized surfaces. *J. Mater. Chem.* **2012**, *22*, 13571–13577.
40. Huwe, H.; Froba, M. Synthesis and characterization of transition metal and metal oxide nanoparticles inside mesoporous carbon CMK-3. *Carbon* **2007**, *45*, 304–314.
41. Hu, Q.Y.; Pang, J.B.; Jiang, N.; Hampsey, J.E.; Lu, Y.F. Direct synthesis of palladium-containing mesoporous carbon. *Microporous Mesoporous Mater.* **2005**, *81*, 149–154.
42. Wan, Y.; Wang, H.Y.; Zhao, Q.F.; Klingstedt, M.; Terasaki, O.; Zhao, D.Y. Ordered mesoporous Pd/silica−carbon as a highly active heterogeneous catalyst for coupling reaction of chlorobenzene in aqueous media. *J. Am. Chem. Soc.* **2009**, *131*, 4541–4550.
43. Su, F.B.; Zeng, J.H.; Bao, X.Y.; Yu, Y.S.; Lee, J.Y.; Zhao, X.S. Preparation and characterization of highly ordered graphitic mesoporous carbon as a Pt catalyst support for direct methanol fuel cells. *Chem. Mater.* **2005**, *17*, 3960–3967.
44. Panels, J.E.; Lee, J.; Park, K.Y.; Kang, S.Y.; Marquez, M.; Wiesner, U.; Joo, Y.L. Synthesis and characterization of magnetically active carbon nanofiber/iron oxide composites with hierarchical pore structures. *Nanotechnology* **2008**, *19*, 455612.
45. Andrada, D.M.; Vieira, H.S.; Oliveira, M.M.; Santos, A.P.; Yin, L.C.; Saito, R.; Pimenta, M.A.; Fantini, C.; Furtado, C.A. Dramatic increase in the Raman signal of functional groups on carbon nanotube surfaces. *Carbon* **2013**, *56*, 235–242.
46. Hirschmann, T.C.; Araujo, P.T.; Muramatsu, H.; Zhang, X.; Nielsch, K.; Kim, Y.A.; Dresselhaus, M.S. Characterization of bundled and individual triple-walled carbon nanotubes by resonant Raman spectroscopy. *ACS Nano* **2013**, *7*, 2381–2387.
47. Vinu, A.; Srinivasu, P.; Takahashi, M.; Mori, T.; Balasubramanian, V.V.; Ariga, K. Controlling the textural parameters of mesoporous carbon materials. *Microporous Mesoporous Mater.* **2007**, *100*, 20–26.
48. Wang, T.; Zhang, C.X.; Sun, X.; Guo, Y.X.; Guo, H.; Tang, J.; Xue, H.R.; Liu, M.Z.; Zhang, X.X.; Zhu, L.; *et al.* Synthesis of ordered mesoporous boron-containing carbon films and their corrosion behavior in simulated proton exchange membrane fuel cells environment. *J. Power Sources* **2012**, *212*, 1–12.

49. Reshetenko, T.V.; Avdeeva, L.B.; Ismagilov, Z.R.; Pushkarev, V.V.; Cherepanova, S.V.; Chuvilin, A.L.; Likholobov, V.A. Catalytic filamentous carbon: Structural and textural properties. *Carbon* **2003**, *41*, 1605–1615.
50. Zhang, P.; Shao, C.L.; Zhang, Z.Y.; Zhang, M.Y.; Mu, J.B.; Guo, Z.C.; Liu, Y.C. *In situ* assembly of well-dispersed Ag nanoparticles (AgNPs) on electrospun carbon nanofibers (CNFs) for catalytic reduction of 4-nitrophenol. *Nanoscale* **2011**, *3*, 3357–3363.
51. Sterk, L.; Górka, J.; Vinu, A.; Jaroniec, M. Soft-templating synthesis of ordered mesoporous carbons in the presence of tetraethyl orthosilicate and silver salt. *Microporous Mesoporous Mater.* **2012**, *156*, 121–126.
52. Liu, P.; Huang, Y.; Wang, L. Ordered mesoporous carbon-reduced graphene oxide composites decorating with Ag nanoparticles for surface enhanced Raman scattering. *Mater. Lett.* **2013**, *97*, 173–176.
53. Xue, Z.; Zhang, F.; Qin, D.; Wang, Y.; Zhang, J.; Liu, J.; Feng, Y.; Lu, X. One-pot synthesis of silver nanoparticle catalysts supported on N-doped ordered mesoporous carbon and application in the detection of nitrobenzene. *Carbon* **2014**, *69*, 481–489.